Differential Hysteresis Modeling of a Shape Memory Alloy Wire Actuator

Sushant M. Dutta, *Student Member, IEEE,* and Fathi H. Ghorbel, *Senior Member, IEEE*

Abstract—In this paper, we develop a complete mathematical model of a shape memory alloy (SMA) wire actuated by an electric current and a bias spring. The operation of the SMA actuator involves different physical phenomena, such as heat transfer, phase transformation with temperature hysteresis, stress–strain variations and electrical resistance variation accompanying the phase transformation. We model each of these phenomena in a modular fashion. A key feature of the proposed model is that one or more of its modules can be extended to fit other SMA applications. At the heart of the proposed model is a differential hysteresis model capable of representing minor hysteresis loops. We generate the temperature profile for the hysteresis model using lumped parameter analysis. We extend the variable sublayer model to represent actuator strain and electrical resistance. This model can be used to develop a position control system for the actuator. Simulation results from the model are found to be in good agreement with experimental data.

Index Terms—Hysteresis, modeling, shape memory alloy (SMA).

I. Introduction

SHAPE memory alloys (SMAs) are metallic alloys which exhibit the shape memory effect, whereby, a shape memory alloy deformed at a low temperature will regain its original undeformed state when heated to a higher temperature. This property is a consequence of the reversible crystalline phase transformation that occurs between the low temperature martensite (M) phase and the high temperature austenite (A) phase of the SMA. The two phases have the same chemical composition but different crystallographic structures, and hence, different thermal, mechanical and electrical properties. The A phase is highly symmetric and usually cubic, while the M phase is non-symmetric and usually monoclinic [1]. In the absence of applied stress, the M phase is formed without any observable macroscopic shape change. However, a large macroscopic inelastic strain can be obtained by applying mechanical stress on the SMA, which forces the M phase variants to *detwin*, i.e., reorient into a single variant. When the SMA is heated to a higher temperature, the M phase returns to the highly symmetric A phase and the inelastic strain is, therefore, recovered. A large force is associated with this strain recovery. The shape memory effect discussed above is called *one way memory effect* (OWME). Apart from M and A phases, the occurrence of another phase, called the R-phase, has also been observed in SMAs [2], [3]. However, the SMA wire used in this research is
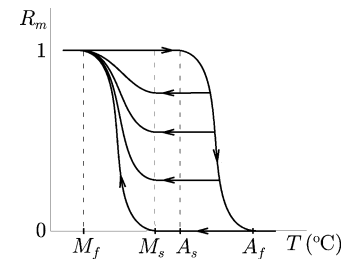
Fig. 1. Schematic of Martensite fraction–temperature hysteresis.

fully annealed near-equiatomic TiNi alloy, and therefore, does not exhibit R-phase [3]. SMAs possess electrical resistance, and it is convenient to heat them using the Joule effect, whereby, an electric current passing through the SMA increases its temperature. Cooling may be accomplished by natural air convection, or using appropriate cooling fluids.

The combination of their high stiffness, high strength, and large recovery strain offers great potential for the use of SMAs as actuators in diverse applications. These include aircraft wing shape control [4], mobile robot actuators [5], microrobot manipulation [6], active endoscopy [7], prosthetic end-effector actuator [8], micro rotary actuator [9], micro fiber switch [10], electrical and mechanical connectors [11], smart structures and composites [12].

The extent of A–M transformation is characterized by the martensite fraction R_m. Martensite fraction is defined as the volume fraction of M phase present in the SMA at any instant. Therefore, $0 \leq R_m \leq 1$. Analogously, one can also define austenite fraction $R_a = 1 - R_m$. In principle, the thermal, mechanical and electrical properties of SMAs can be predicted if R_m and the stress history of the SMA are known. However, it is not possible to measure R_m by nondestructive means [13]. Differential scanning calorimetry (DSC) is a well-known method for analyzing phase transformations, and it has been shown that the A–M transformation exhibits significant temperature hysteresis [2]. A typical martensite fraction–temperature hysteresis schematic is shown in Fig. 1. The transformation is characterized by the transformation start and finish temperatures. A_s and A_f are the start and finish temperatures for A phase, respectively, while M_s and M_f are the start and finish temperatures for M phase, respectively.

Most of the SMA actuator applications mentioned earlier in this section use SMA wires, because they are easy to cut, to connect, and to activate electrically. It is common to obtain an inelastic strain in M phase by virtue of a bias spring connected in series with the SMA wire. Thus, the wire contracts when heated, and it expands with the aid of the bias spring when cooled. A
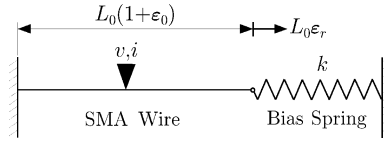
Fig. 2. Schematic of spring-biased SMA wire actuator.

Fig. 3. Proposed modular system block diagram.

schematic of a spring-biased SMA wire actuator is shown in Fig. 2. In this paper, we propose a complete mathematical model of this spring-biased SMA wire actuator.

This paper uses experimental results obtained by Ma *et al.* [1] on their experimental setup for spring-biased SMA wire actuator. Here, we give only an outline of the measurement and actuation system of the setup. The details of the experimental setup are given in [1]. A potential difference $v(t)$ is applied across the SMA wire using a programmable power supply. This causes an electric current $i(t)$ to flow through the SMA wire, which gets heated up via the Joule effect. Both $v(t)$ and $i(t)$ are measurable in real time. Therefore, power vi and electrical resistance $R = v/i$ can also be computed in real-time. The output is ϵ_r, which is the recoverable strain caused by the SMA deformation. The actual strain is measured using a linear variable differential transformer (LVDT).

A common requirement in SMA actuator applications is to control ϵ_r to follow a desired strain $\epsilon_{rd}(t)$. One way to do this is to measure the actual strain and minimize the strain error using a closed-loop control scheme. However, strain measurement could be expensive [1] or impractical [14]. The other method is to use a mathematical model of the actuator either as an estimator, or for model-based control. This is the motivation behind this work.

While new applications for SMA actuators have been prolifically developed over the years, their mathematical modeling for real-time control remains an open research problem. We list some important developments here. The *variable sublayer model*, proposed by Ikuta *et al.* [2], hypothesizes that SMAs consist of parallel connected sublayers of different phases with different mechanical characteristics. Brailovski *et al.* [15] used a lumped parameter convective heat transfer equation to generate the temperature profile for SMAs, given the voltage and the current. Madill and Wang [16] also used the same equation, assuming constant parameters. They extended the work of [2] to model a SMA wire actuator under constant load and used the model to propose an L2-stable position proportional control system. However, it has been shown that the parameters in the heat transfer equation are temperature-dependent [17], [18]. Recently, Ma *et al.* [1] used a neural network model of $R(t)$–$\epsilon_r(t)$ for position proportional integral derivative (PID) control of a spring-biased SMA wire actuator. However, they did not model minor hysteresis loops.

Hysteresis modeling in SMAs has been studied extensively in the literature, and forms a significant part of the SMA actuator modeling literature. Bo and Lagoudas [13] provide a comprehensive review of hysteresis modeling in SMAs. The Preisach model has been widely used to model SMA hysteresis. However, it has been pointed out that the Preisach model is unable to represent dead zones of transformation or drift of hysteresis loops with cyclic loading during partial transformation [19].
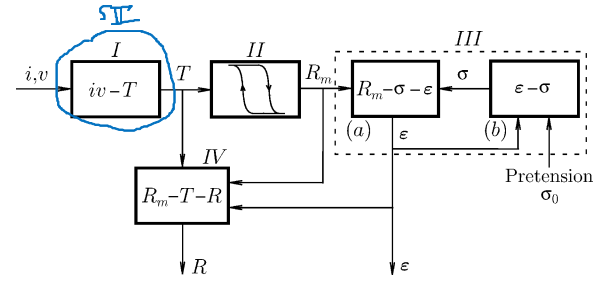
Also, computation of the weighting function for every point in the hysteresis region is a tedious process. Many other algebraic models for SMA hysteresis have also been developed [13], [2], [16], [19], [20]. From the control systems point of view, it is advantageous to model the hysteresis using a differential model. Then, the hysteresis model can easily be incorporated into the SMA dynamics state space equations. A differential hysteresis model also facilitates the stability analysis of the system. Yet, there is a lack of differential models of SMA hysteresis in the literature. Likhachev [21] proposed a general differential model for representing SMA hysteresis minor loops, which is probably the only differential model of SMA hysteresis in the literature.

In this paper, we follow a modular approach to modeling each system element of the spring-biased SMA wire actuator. Our approach is summarized in Fig. 3. We make four main contributions.

1) We use temperature-dependent parameters in the lumped parameter convective heat transfer equation to obtain accurate temperature profile. (Fig. 3, module *I*)
2) We propose particular functions for Likhachev's general differential hysteresis model [21] to model the major and minor loops for martensite fraction–temperature hysteresis. (Fig. 3, module *II*)
3) We extend Madill and Wang's [16] strain analysis for SMA wire actuator under constant load to spring-biased SMA wire actuator. (Fig. 3, modules *III(a)* and *III(b)*)
4) We use the variable sublayer model [2] to model SMA resistance. We propose nonlinear temperature coefficients of resistivity for each phase. Modeling of SMA resistance has significant applications. For example, the electrical resistance of a SMA wire may be used to detect the crack propagation in a SMA composite [14]. (Fig. 3, module *IV*)

The remainder of the paper is organized as follows. Section II describes the heat transfer problem and the computation of the temperature profile. Section III presents the martensite fraction–temperature hysteresis differential model. Section IV establishes the actuator strain as a function of pretension and martensite fraction. Section V describes electrical resistance calculations. Section VI discusses parameter identification and simulation results. In Section VII, we present our conclusions.

II. HEAT TRANSFER AND TEMPERATURE

In this section, we describe the heat transfer problem of the SMA wire and develop the temperature profile for the SMA wire. This constitutes module *I* of Fig. 3.

The system gains heat energy from electrical power, and loses part of it to the environment. The balance of the heat energy

governs the temperature of the SMA wire. A straightforward method for solving this transient heat transfer problem is the lumped parameter analysis, whereby, it is assumed that the internal resistance of the wire to heat conduction is negligible compared to the convective heat transfer with the environment. This assumption is valid for heat transfer in thin metal samples [15]. We also assume that only natural convection occurs. Let

ρ mass density of SMA wire [kgm^{-3}];

c specific heat of SMA wire [Jkg^{-1}°C^{-1}];

L_0 undeformed SMA wire length in 100% A state [m];

d_0 cross-sectional diameter of undeformed SMA wire [m];

ϵ_0 strain caused by pretension load in 100% A state;

ϵ_r strain caused by A–M phase transformation;

ϵ = $\epsilon_0 + \epsilon_r$, total strain;

h convection heat transfer coefficient [Wm^{-2}°C^{-1}];

v voltage across SMA wire [V];

i current through SMA wire [A];

T_{amb} ambient temperature [°C].

Then, the temperature T [°C] of the SMA wire is governed by the following lumped parameter convective heat transfer equation:

$$\rho c \frac{\pi d_0^2 L_0}{4} \frac{dT}{dt} = vi - \pi d_0 L_0 \left(1 + \frac{\epsilon}{2}\right) h(T - T_{\text{amb}})$$
$$\approx vi - \pi d_0 L_0 h(T - T_{\text{amb}}). \quad (1)$$

Madill and Wang [16] used the above equation assuming that both h and c are constants. However, h is, in general, temperature dependent [17] and, for SMAs, c is also temperature dependent [18]. It was found that the following expressions for h and c satisfy experimental results:

$$h = \begin{cases} a_1 - a_2 T, & \dot{T} \geq 0 \\ a_3 + a_4 \, \text{erf}\left(\frac{T - m_1}{n_1}\right), & \dot{T} < 0 \end{cases} \quad (2)$$

$$c = b_1 + b_2 \, \text{erf}\left(\frac{T - m_2}{n_2}\right) \quad (3)$$

where a_1, a_2, a_3, a_4, b_1, b_2, m_1, n_1, m_2, and n_2 are constant parameters. Fig. 4 shows the temperature profile (solid lines) obtained from (1) corresponding to a sinusoidal voltage input with decreasing amplitude (dashed lines) [1]. Strain calculations in Section IV show that for the simulations in this work, the value of ϵ does not exceed 0.105. Thus, we are justified in neglecting the $\epsilon/2$ term in (1).

Since the actual temperature was not measured in the experimental setup, direct validation of the heat transfer model was not possible. It is worth noting that, while (1) has a physical basis, the functions in (2) and (3) are obtained phenomenologically. We justify the validity of (1)–(3) by the following arguments.

It is known that M–A transformation is exothermic, while A–M transformation is endothermic [22]. Transformation temperatures A_s and M_s are shown in Fig. 4. The decrease in slope above A_s represents the exothermic transformation, while the decrease in slope below M_s represents the endothermic transformation. Further, as shown in Fig. 5, when the strain (dashed lines) decreases, the temperature (solid lines) increases. While the strain is constant at its minima, the temperature decreases. When the strain increases, the temperature decreases further.
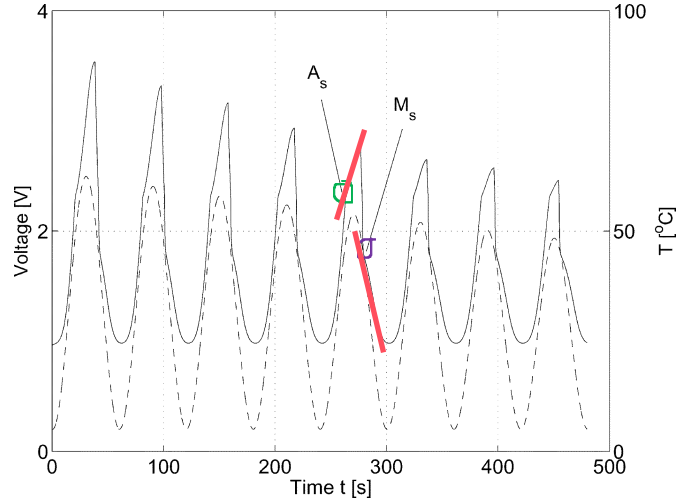

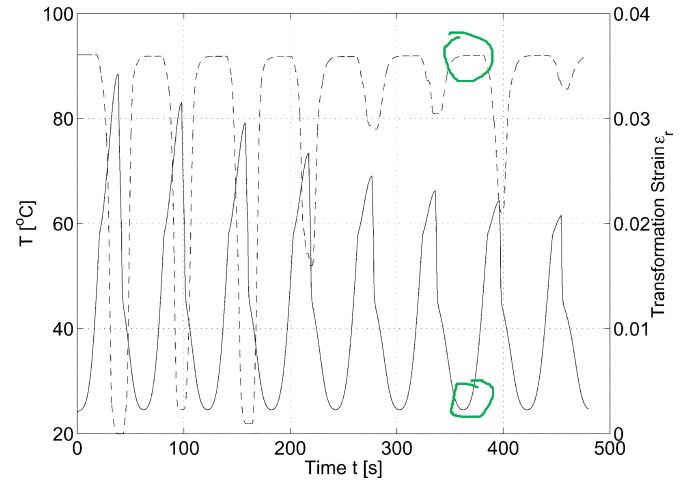Fig. 4. Input voltage and simulated temperature profiles.

Fig. 5. Simulated temperature and measured transformation strain profiles.

While the strain is constant at its maxima, the temperature increases. This is exactly as observed experimentally [21].

In this section, we developed the temperature profile for the SMA wire actuator as a function of the input electrical power and time. As Fig. 3 shows, this is module I of the proposed system model, and thus, forms the basis for the remainder of the paper. Some important issues regarding the development of the temperature profile will be discussed in Section VI.

III. MARTENSITE FRACTION–TEMPERATURE HYSTERESIS

The A–M transformation, and hence the relationship between R_m and T, is hysteretic. In this section, we propose special functions for the general differential hysteresis model proposed by Likhachev [21] and delineate the formulation of the martensite fraction–temperature (R_m–T) differential hysteresis model, which forms module II of Fig. 3.

The typical R_m–T hysteretic relationship is shown schematically in Fig. 1. The hysteresis loop corresponding to complete A–M transformation is called the major hysteresis loop. Incomplete A–M transformation yields minor hysteresis loops within the major hysteresis loop. The shape and transformation temperatures of minor loops are the same as those of the major loop [2],

[16], [19]. It is known that transformation temperatures change with applied stress [23]. However, stress calculations in Section IV show that the stress variation throughout the operation of the actuator is merely 4 MPa, which implies a variation of less than 1 °C in the transformation temperatures. Hence, we assume that M_f, M_s, A_s, and A_f are constant throughout.

We follow a phenomenological approach to hysteresis modeling in this section. The proposed hysteresis model is a *Duhem* [24] differential model. Consider an input (independent) variable $u(t)$, an output (dependent) variable $v(t)$, and a hysteresis relationship on the $u(t)$–$v(t)$ input-output plane. The Duhem model follows intuitively from the fact that if $u(t)$ is an increasing function, then $v(t)$ increases along one path, and if $u(t)$ is a decreasing function, then $v(t)$ decreases along another path, the slopes of the paths being given by functions g_+ and g_-, respectively. Mathematically, the Duhem model is given by

$$\begin{cases} \dot{v} &= g_+(u(t),v(t))(\dot{u})^+ - g_-(u(t),v(t))(\dot{u})^- \\ v(0) &= v_0 \end{cases} \quad (4)$$

where $(\dot{u})^{\pm} = (|\dot{u}| \pm (\dot{u}))/2$ and $g_+, g_- \in C^0(\mathbb{R}^2)$ [24]. We will refer to g_+ and g_- as *slope functions*.

We first consider the major loop, and then the minor loops. We propose to use Gaussian probability density functions (PDFs) as the slope functions of the major loop. A Gaussian PDF is characterized by its mean μ and the variance σ^2. Hence

$$g_{+/-}(u) = \frac{1}{\sigma_{+/-}\sqrt{2\pi}} \exp\left(-\frac{(u - \mu_{+/-})^2}{2\sigma_{+/-}^2}\right) \quad (5)$$

where subscripts $+$ and $-$ denote increasing and decreasing curves, respectively. Then, the output v representing the major loop is given by

$$v_{+/-} = h_{+/-}(u) = \int_{-\infty}^{u} g_{+/-}(u')du'$$

$$= \frac{1}{2}\left[1 + \operatorname{erf}\left(\frac{u - \mu_{+/-}}{\sigma_{+/-}\sqrt{2}}\right)\right]. \quad (6)$$

Hence, the major loop is given by the differential equation

$$\frac{dv}{du} = \begin{cases} \frac{1}{\sigma_+\sqrt{2\pi}} \exp\left(-\frac{(u-\mu_+)^2}{2\sigma_+^2}\right), & \dot{u} \geq 0 \\ \frac{1}{\sigma_-\sqrt{2\pi}} \exp\left(-\frac{(u-\mu_-)^2}{2\sigma_-^2}\right), & \dot{u} < 0. \end{cases} \quad (7)$$

We observe that the minor loop slope functions can be obtained by multiplying the major loop slope functions in (5) by a suitable scaling constant $n_{i_{+/-}} \in [0,1]$, where $i = 1 \ldots N$, whence, we get

$$g_{i_{+/-}}(u) = \frac{n_{i_{+/-}}}{\sigma_{+/-}\sqrt{2\pi}} \exp\left(-\frac{(u - \mu_{+/-})^2}{2\sigma_{+/-}^2}\right) \quad (8)$$

which are the slope functions for the ith minor loop. Typical slope functions for $i = 1,2,3$ are shown in Fig. 6. The corresponding minor loop curves are shown in Fig. 7. Note that $n_{i_{+/-}} = 1$, in fact, gives the major loop.

It is evident that the hysteresis loops in Fig. 7 would qualitatively match the hysteresis loops in Fig. 1 if the y axis were inverted. This justifies the use of Gaussian PDFs as slope functions.
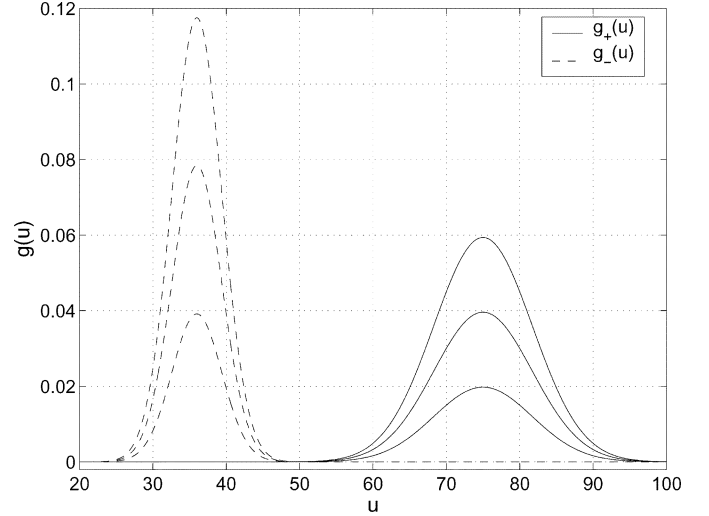

Fig. 6.   Scaled Gaussian PDFs as slope functions for hysteresis loops.
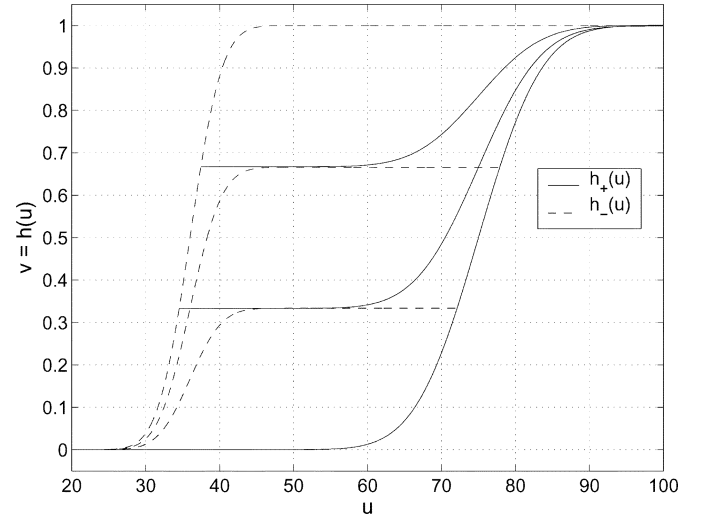

Fig. 7.   Integrals of Gaussian PDFs yield hysteresis loops.

To obtain a differential model for minor hysteresis loops, it remains to be shown that the scaling constants for each minor curve at any time instant t can be expressed in terms of the couple $(u(t), v(t))$. We refer to Fig. 8. $h_{+/-}(u)$ is the major loop, $h_{1_-}(u)$ and $h_{2_-}(u)$ are minor loop decreasing curves, $g_{+/-}(u)$ is the slope of the major loop and $g_{1_-}(u,v)$ and $g_{2_-}(u,v)$ are slope functions of the minor loop decreasing curves. We observe that scaling constant n_{1_-} can be expressed as

$$n_{1_-}(u,v) = \frac{b}{a+b} = \frac{h_{1_-}(u) - h_+(u)}{h_-(u) - h_+(u)} = \frac{v - h_+(u)}{h_-(u) - h_+(u)}. \quad (9)$$

Therefore, the slope function g_{1_-} becomes

$$g_{1_-}(u,v) = \frac{v - h_+(u)}{h_-(u) - h_+(u)} g_-(u). \quad (10)$$

A similar analysis can be done for increasing curves. Thus, the complete differential hysteresis model can be expressed as

$$\frac{dv}{du} = \begin{cases} \frac{h_-(u)-v}{h_-(u)-h_+(u)} g_+(u), & \dot{u} \geq 0 \\ \frac{v-h_+(u)}{h_-(u)-h_+(u)} g_-(u), & \dot{u} < 0. \end{cases} \quad (11)$$
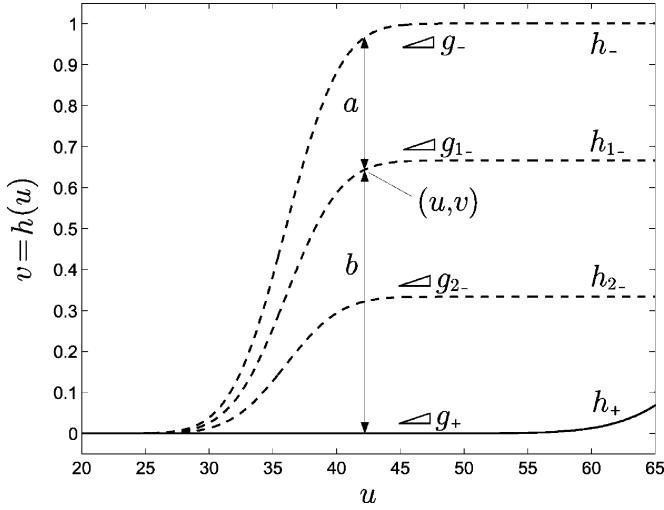
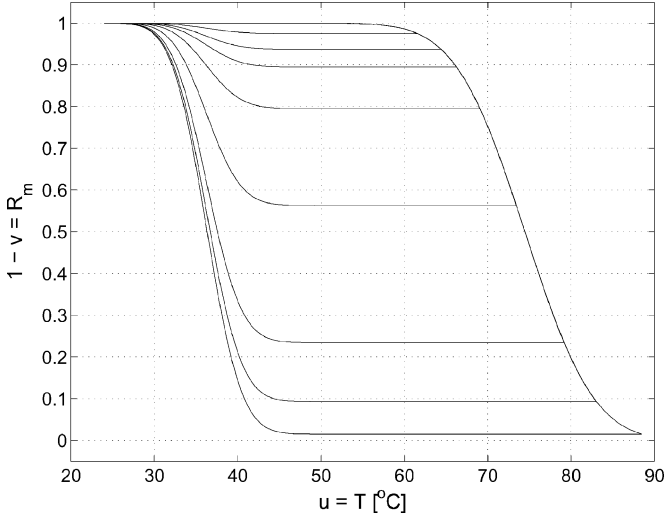Fig. 8.   Method for obtaining differential model for minor loops.

Fig. 9.   Simulated Martensite fraction versus temperature hysteresis plot.

We put $u = T$ and $v = R_a$ in (11) to obtain the R_a–T hysteresis model. Putting $1 - v = R_m$ yields the R_m–T hysteresis model

$$\begin{cases} \dfrac{dR_m}{dT} = \begin{cases} \dfrac{h_-(T) + R_m - 1}{h_+(T) - h_-(T)} g_+(T), & \dot{T} \geq 0 \\[2mm] \dfrac{h_+(T) + R_m - 1}{h_-(T) - h_+(T)} g_-(T), & \dot{T} < 0 \end{cases} \\ R_m(0) = 1 \end{cases} \quad (12)$$

where $g_{+/-}$ and $h_{+/-}$ are given by (5) and (6), respectively.

Scaling constants for minor hysteresis loops given in (11) were originally proposed by Likhachev [21]. Fig. 9 shows the hysteresis loops obtained from (12) for the temperature profile shown in Fig. 4. Hence, (12) gives the complete martensite fraction-temperature differential hysteresis model, which forms module *II* of the proposed system model of Fig. 3. Later in this paper, we will use (12) to model the SMA wire strain and electrical resistance as functions of temperature.
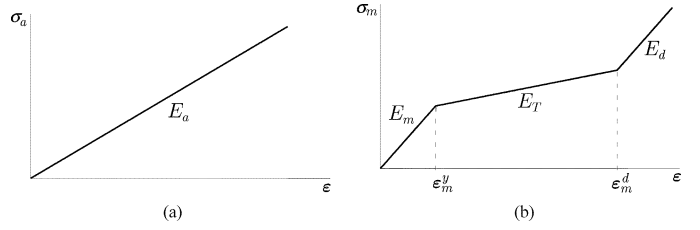

Fig. 10.   Schematic stress versus strain curves. (a) Austenite. (b) Martensite.

IV. STRESS AND STRAIN

In this section, we extend the SMA strain results derived by Madill and Wang [16] to the case of the spring-biased SMA wire actuator, and derive ϵ as an explicit function of R_m. This forms module *III* of Fig. 3. The treatment follows Madill and Wang [16]. Let

σ_0 pretension load stress due to bias spring [MPa];
Δ spring deformation in 100% austenitic state [m];
σ_a stress due to 100% austenite [MPa];
σ_m stress due to 100% martensite [MPa];
E_a elasticity of austenite [MPa];
E_m elasticity of fully twinned martensite [MPa];
E_T elasticity of partly twinned martensite [MPa];
E_d elasticity of detwinned martensite [MPa];
ϵ_m^y yield strain of twinned martensite;
ϵ_m^d minimum strain of detwinned martensite;
k bias spring constant [Nm^{-1}].

The pretension load stress σ_0 is given by

$$\sigma_0 = E_a \epsilon_0 = \frac{4k\Delta}{\pi d_0^2(1 - \epsilon_0)}. \quad (13)$$

Therefore, the prestrain ϵ_0 is given by

$$\epsilon_0 = \frac{1}{2} - \frac{1}{2}\sqrt{1 - \frac{16k\Delta}{\pi d_0^2 E_a}}. \quad (14)$$

Also, elongation of the wire causes some spring relaxation, which in turn causes the tensile load on the wire to decrease below σ_0

$$\sigma = \frac{4k(\Delta - L_0\epsilon_r)}{\pi d_0^2(1 - \epsilon)} = \frac{4k(\Delta - L_0\epsilon_r)}{\pi d_0^2(1 - \epsilon_0 - \epsilon_r)}. \quad (15)$$

According to the variable sublayer model [2], the tensile load σ gets distributed in the two phases, and is given by

$$\sigma = (1 - R_m)\sigma_a + R_m\sigma_m \quad (16)$$

where σ_a and σ_m are obtained from the stress–strain characteristics of A phase and M phase, respectively, shown in Fig. 10 [16]. Eliminating σ from (15) and (16), we get

$$\epsilon = \begin{cases} \epsilon_0 - \dfrac{d_1}{2c_1} - \dfrac{\sqrt{d_1^2 - 4c_1 e_1}}{2c_1}, & \text{if } 0 \leq \epsilon < \epsilon_m^y \\[2mm] \epsilon_0 - \dfrac{d_2}{2c_2} - \dfrac{\sqrt{d_2^2 - 4c_2 e_2}}{2c_2}, & \text{if } \epsilon_m^y \leq \epsilon < \epsilon_m^d \\[2mm] \epsilon_0 - \dfrac{d_3}{2c_3} - \dfrac{\sqrt{d_3^2 - 4c_3 e_3}}{2c_3}, & \text{if } \epsilon_m^d \leq \epsilon \end{cases} \quad (17)$$
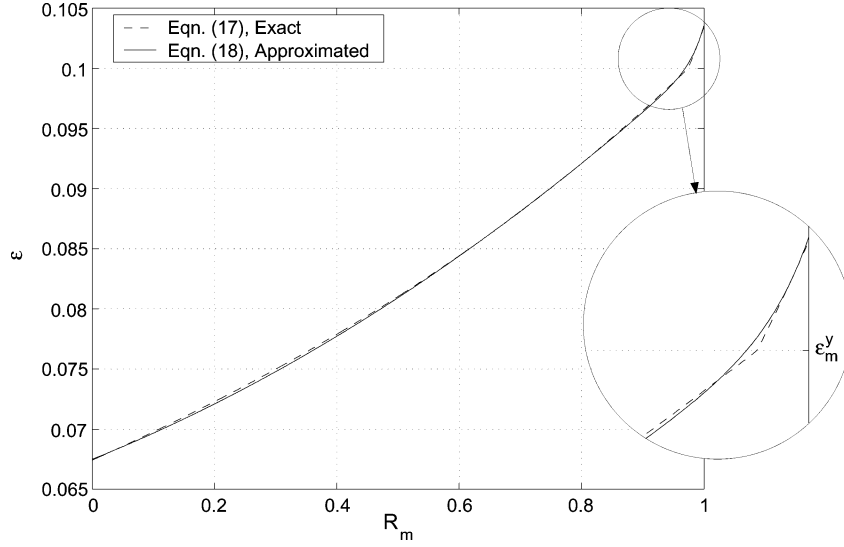
Fig. 11.   Simulated strain versus Martensite fraction plot.

where c_i, d_i, and e_i ($i = 1,2,3$) are given in the Appendix . For the simulations in this paper, $\epsilon < \epsilon_m^d$ always. The expression in (17) is only piecewise differentiable. We approximate it to a polynomial in R_m in order to obtain a continuously differentiable expression for ϵ in the range $\epsilon_0 \le \epsilon < \epsilon_m^d$:

$$\epsilon = \epsilon_0 + k_1 R_m + k_2 R_m^2 + k_3 R_m^{50} \tag{18}$$

where k_1, k_2 and k_3 are constant parameters. The above expression is obtained using MATLAB's curve fitting toolbox. For typical parameter values, the strain values obtained from (17) and the approximated strain obtained from (18) are shown in Fig. 11.

In this section, we extended the work of Madill and Wang [16] to obtain the strain in the SMA wire actuator as an explicit function of martensite fraction. As shown in Fig. 3, this result forms module *III* of the proposed system model. It will be combined with the R_m–T hysteresis model developed in the previous section to model the SMA wire strain versus temperature relationship. Simulation results are presented in Section VI.

V. ELECTRICAL RESISTANCE

In this section, we model the electrical resistance of the SMA wire as a function of R_m, T, and ϵ using the variable sublayer model [2]. This forms module *IV* of Fig. 3. Let

$R_{A/M}$ electrical resistance of 100% A/M phase [Ω];
$\rho_{A/M}(T)$ electrical resistivity of A/M phase [Ωm].

Then, the electrical resistance of each phase is given by

$$R_{A/M} = \frac{4L_0(1 + 2\epsilon)}{\pi d_0^2} \rho_{A/M}(T). \tag{19}$$

Using the variable sublayer model [2], the two phases can be considered to be in parallel. Then, the SMA wire electrical resistance R is given by

$$\frac{1}{R} = \frac{(1 - R_m)}{R_A} + \frac{R_m}{R_M}. \tag{20}$$

Substituting for R_A and R_M from (19), we obtain

$$\frac{1}{R} = \frac{\pi d_0^2}{4L_0(1 + 2\epsilon)} \left[\frac{1 - R_m}{\rho_A(T)} + \frac{R_m}{\rho_M(T)} \right]. \tag{21}$$
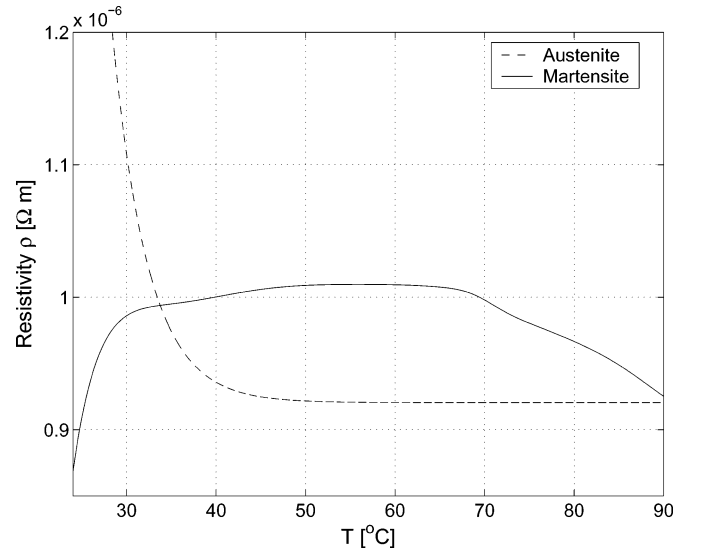

Fig. 12.   Simulated electrical resistivity versus temperature plot.

Ikuta *et al.* [2] modeled the resistivities as linear functions of temperature. However, we find that the following nonlinear expressions for the resistivities satisfy experimental results:

$$\rho_A(T) = p_1 + p_2 \exp\left(-p_3(T - T_{\mathrm{amb}})\right) \tag{22}$$

$$\rho_M(T) = (q_1 - q_2 T) \left[1 + \mathrm{erf}\left(\frac{T - m_3}{n_3}\right) \right]$$

$$+ \sum_{i=0}^{i=9} \alpha_i (T - T_{\mathrm{amb}})^i \tag{23}$$

where p_1, p_2, p_3, q_1, q_2, m_3, n_3, and α_i ($i = 0, \ldots, 9$) are constant parameters. The nonlinear resistivity functions computed from (22) and (23) are plotted in Fig. 12. These functions are obtained phenomenologically, as follows. Consider Fig. 1 and Fig. 9. Suppose $T \in [M_f, A_s]$. Then, $R_m = 1$ and R would only depend on ρ_M. Thus, ρ_M should take a form which would yield the shape of the major loop increasing curve in Fig. 13. Similarly, ρ_A should take a form which would yield the shape

TABLE I
SIMULATION PARAMETERS

ρ	6500 kgm^{-3}	T_{amb}	24 °C
L_0	0.2286 m	d_0	3.81×10^{-4} m
a_1	165 Wm$^{-2\circ}$C^{-1}	b_1	1400 Jkg$^{-1\circ}$C^{-1}
a_2	0.5 Wm$^{-2\circ}$C^{-2}	b_2	1000 Jkg$^{-1\circ}$C^{-1}
a_3	300 Wm$^{-2\circ}$C^{-1}	m_1	48 °C
a_4	150 Wm$^{-2\circ}$C^{-1}	m_2	58 °C
n_1	10 °C	n_2	0.5 °C
μ_+	78.9 °C	σ_+	11.2 °C
μ_-	34 °C	σ_-	5.8 °C
Δ	0.04425 m	k	58.19 Nm^{-1}
E_a	35917 MPa	E_m	20480 MPa
E_T	826 MPa	E_d	16800 MPa
ϵ_m^y	0.1	ϵ_m^d	0.15
k_1	0.0204	k_2	0.01293
k_3	0.0027		
p_1	9.2×10^{-7} Ωm	q_1	3.4×10^{-8} Ωm
p_2	8.4×10^{-7} Ωm	q_2	5.7×10^{-10} Ωm°C^{-1}
p_3	0.2499 °C^{-1}	m_3	70 °C
n_3	3 °C		
α_0	8.7×10^{-7} Ωm	α_1	4.8×10^{-8} Ωm°C^{-1}
α_2	-7.8×10^{-9} Ωm°C^{-2}	α_3	7.0×10^{-10} Ωm°C^{-3}
α_4	-3.7×10^{-11} Ωm°C^{-4}	α_5	1.2×10^{-12} Ωm°C^{-5}
α_6	-2.5×10^{-14} Ωm°C^{-6}	α_7	3.2×10^{-16} Ωm°C^{-7}
α_8	-2.2×10^{-18} Ωm°C^{-8}	α_9	6.7×10^{-21} Ωm°C^{-9}

Fig. 13. Electrical resistance versus temperature.

Fig. 14. Strain versus temperature.

of the major loop decreasing curve in Fig. 13. The above reasoning explains qualitatively why the temperature dependence of resistivities of each phase is as shown in Fig. 12. The specific forms in (22) and (23) are obtained using MATLAB's curve fitting toolbox.

This result will be used in conjunction with the hysteresis model developed in Section III to model the SMA wire resistance versus temperature relationship. Section VI shows simulation results.

VI. PARAMETER IDENTIFICATION AND RESULTS

In this section, we present parameter identification for the proposed model and simulation results from the proposed model and their comparison with the experimental data of [1].

Table I shows the parameter values used in this modeling study. Parameters used in (1) and (17) are either obtained empirically, or taken from literature [16]. First estimates for parameters used in (18) were obtained by curve fitting (18) to (17). The remaining parameters were identified using the actual strain and electrical resistance measurements, since the actual temperature measurements were not available, and martensite fraction measurements were not possible. Parameters used in (2), (3), (5), (18), (22), and (23) were obtained by nonlinear least-squares optimization. This was accomplished in MATLAB using the Levenberg–Marquardt algorithm [25] and with strain and electrical resistance errors as the objective functions. The starting values of the parameters for the optimization algorithm were obtained by hand tuning.

Figs. 13 and 14 show the simulation results for SMA electrical resistance and transformation strain and their comparison with experimental results. In both figures, even for the plots titled "experimental," the quantity on the x axis is the simulated temperature. It has already been pointed out that actual temperature was not measured in the experimental setup. We choose
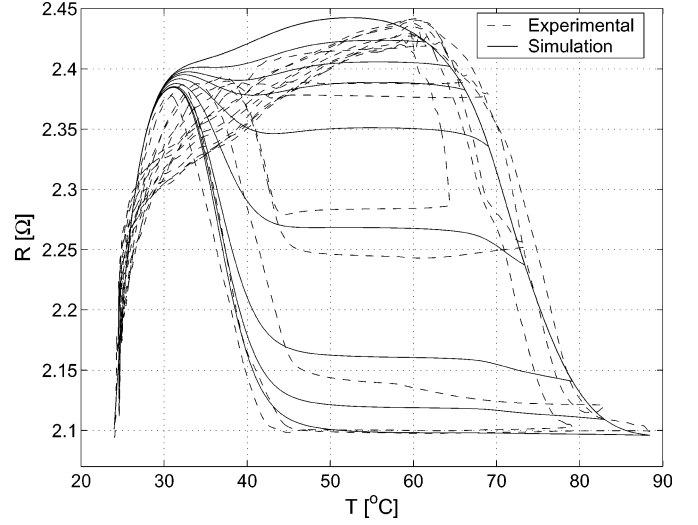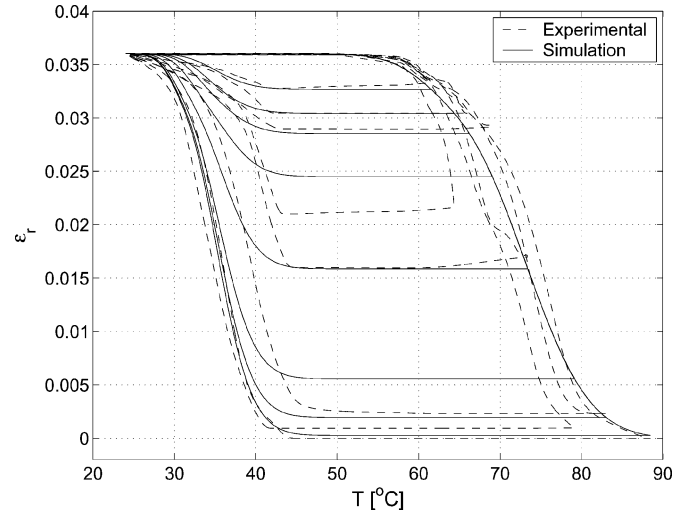
temperature as the x axis to clearly illustrate the dynamics of strain and electrical resistance as compared to the Martensite fraction–temperature hysteresis.

Finally, the ϵ_r–R relation is plotted in Fig. 15. Ma *et al.* [1] used a neural network model of the ϵ_r–R major loop to achieve position PID control of spring-biased SMA wire actuator. Fig. 15 shows that the proposed model is capable of modeling ϵ_r–R minor loops as well, and therefore, may be used to achieve more accurate position control of the actuator with resistance feedback.

It can be seen from Figs. 13–15 that the simulation results from the proposed model are in qualitative agreement with the experimental results. The discrepancy between simulated and experimental data can be explained as follows. The measured transformation strain shown in Fig. 5 corresponds to the voltage profile of Fig. 4. Thus, the strain amplitude should gradually decrease with each voltage cycle. However, Fig. 5 shows significant anomalies in the measured strain profile. These can be attributed to the fact that the ambient conditions of the experimental setup are not constant over time and space, since the ex-
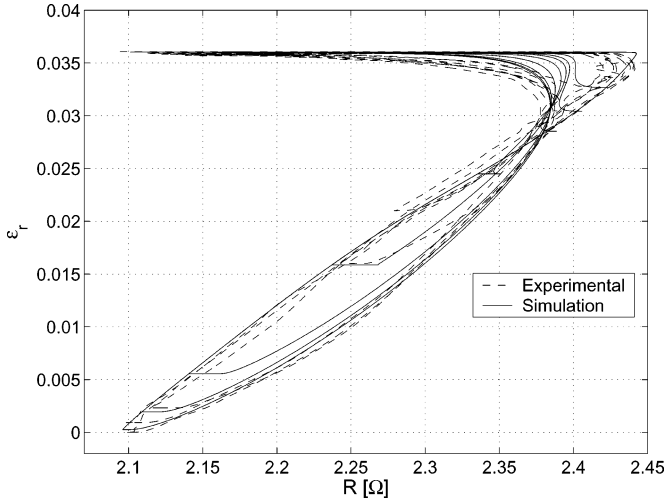
Fig. 15.   Strain versus electrical resistance.

perimental setup is not contained in a hermetically sealed enclosure and the natural convection assumption made in Section II does not strictly hold. Another source of error is that the functions in (2) and (3) were obtained empirically from the measured transformation strain, since the actual temperature data was not available. Hence, there is an unavoidable error in the simulated temperature profile, which is carried over to modules *II*, *III*, and *IV*. Additionally, it is common for a film of Titanium Oxide to form at the contacts of the SMA wire over time, which introduces extraneous electrical resistance into the circuit. The shorter the length of the SMA wire, the higher the error due to Titanium Oxide resistance. It has also been pointed out by Ma *et al.* [1] that the experiments conducted on the SMA wire do not exhibit accurate repeatability until it has been subjected to sufficient thermal cycling. Hence, the simulation results should be viewed in light of the above issues.

It is evident that the actuator behavior is highly nonlinear due to the complex physics of the SMA. There have been several physics-based thermomechanical models of SMAs (for example [13], [19]), which have not found use in the control of SMA actuators due to their complicated nature. Preisach models have found widespread use in SMA modeling, but their limitations have been mentioned in Section I. The proposed model does not suffer from these limitations. It is computationally simple, enabling inexpensive real-time control of the SMA wire actuator. The above discussion demonstrates the effectiveness of our modeling study.

VII. CONCLUSION

In this paper, we developed a complete mathematical model for a spring-biased shape memory alloy wire actuator. The model is capable of simulating the temperature, martensite fraction, stress, strain and electrical resistance of the actuator. We used lumped parameter analysis to obtain the temperature profile. We proposed particular functions for Likhachev's general differential hysteresis equations [21] to represent major and minor hysteresis loops. The model also extends the variable

sublayer model to obtain strain and electrical resistance of the actuator.

One or more modules of the model can be extended to other applications. For example, the hysteresis and electrical resistance modules may be used to detect the crack propagation in a SMA composite [14]. The ϵ_r–R simulation in Fig. 15 can facilitate resistance feedback position control applications such as [1]. A salient feature of the proposed model is that it is built upon a differential hysteresis model. The differential hysteresis model proposed in Section III uses only four parameters to generate major and minor loops for any temperature profile. This presents a significant advantage over algebraic models which require new parameter values in each thermal half-cycle (for example, [16]). We have also shown that the proposed differential hysteresis model represents the dead zone of phase transformation (Fig. 1, region between M_s and A_s), and is, in that sense, superior to the Preisach model. Furthermore, the proposed differential hysteresis model makes it convenient to obtain a state space model of the SMA actuator. It facilitates the use of the rich theory of ordinary differential equations for analysis. It is also feasible to construct an inverse of the differential hysteresis model for inverse compensation of hysteresis.

We also discussed significant issues regarding temperature modeling of SMAs. This discussion yields a direction for enhancement of the proposed model. The proposed model can be refined if actual temperature of the SMA wire is measured during experiments and the heat transfer model is validated using this data. Further, by placing the experimental setup in a hermetically sealed enclosure, the temperature profile can be much better controlled, which would obviously yield more accurate results.

APPENDIX

The parametric variables in (17) are given by

$$c_1 = \pi d_0^2 [E_a + (E_m - E_a)R_m]$$
$$d_1 = -4kL_0 - \pi d_0^2[E_a + (E_m - E_a)R_m](1 - 2\epsilon_0)$$
$$e_1 = 4k\Delta - \pi d_0^2[E_a + (E_m - E_a)R_m]\epsilon_0(1 - \epsilon_0)$$
$$c_2 = \pi d_0^2[E_a + (E_T - E_a)R_m]$$
$$d_2 = -4kL_0 - \pi d_0^2[E_a + (E_T - E_a)R_m](1 - 2\epsilon_0)$$
$$\quad + \pi d_0^2 R_m \epsilon_m^y(E_m - E_T)$$
$$e_2 = 4k\Delta - \pi d_0^2(1 - \epsilon_0)[E_a\epsilon_0 + (E_T - E_a)R_m\epsilon_0$$
$$\quad + (E_m - E_T)R_m\epsilon_m^y$$
$$c_3 = \pi d_0^2[E_a + (E_d - E_a)R_m$$
$$d_3 = -4kL_0 - \pi d_0^2[E_a + (E_d - E_a)R_m](1 - 2\epsilon_0)$$
$$\quad + \pi d_0^2 R_m[(E_m - E_T)\epsilon_m^y + (E_T - E_d)\epsilon_m^d]$$
$$e_3 = 4k\Delta - \pi d_0^2(1 - \epsilon_0)[E_a\epsilon_0 + (E_d - E_a)R_m\epsilon_0$$
$$\quad + (E_m - E_T)R_m\epsilon_m^y + (E_T - E_d)R_m\epsilon_m^d].$$

REFERENCES

[1] N. Ma, G. Song, and H.-J. Lee, "Position control of shape memory alloy actuators with internal electrical resistance feedback," in *Proc. SPIE*, vol. 5049, 2003, pp. 46–55.

[2] K. Ikuta, M. Tsukamoto, and S. Hirose, "Mathematical model and experimental verification of shape memory alloy for designing micro actuator," in *Proc. IEEE Microelectromechanical Systems*, Jan.-Feb. 1991, pp. 103–108.

[3] T. Saburi, *Shape Memory Materials*. Cambridge, U.K.: Cambridge Univ. Press, 1998, ch. 3, pp. 49–96.

[4] J. Kudva, B. Sanders, J. Pinkerton-Florance, and E. Garcia, "Overview of the DARPA/AFRL/NASA smart wing Phase 2 program," in *Proc. SPIE*, vol. 4332, 2001, pp. 383–389.

[5] M. Hashimoto, M. Takeda, H. Sagawa, I. Chiba, and K. Sat, "Shape memory alloy and robotic actuators," *J. Robot. Syst.*, vol. 2, no. 1, pp. 3–25, 1985.

[6] K.-Y. Tu, T.-T. Lee, C.-H. Wang, and C.-A. Chang, "Design of a fuzzy walking pattern (FWP) for a shape memory alloy (SMA) biped robot," *Robotica*, vol. 17, no. 4, pp. 373–382, 1999.

[7] K. Ikuta, M. Tsukamoto, and S. Hirose, "Shape memory alloy servo actuator system with electric resistance feedback and application for active endoscope," in *Proc. IEEE Int. Conf. Robotics and Automation*, vol. 1, 1988, pp. 427–430.

[8] M. Bergamasco, F. Salsedo, and P. Dario, "Shape memory alloy micromotors for direct-drive actuation of dexterous artificial hands," *Sensors Actuat.*, vol. 17, no. 1, pp. 115–119, 1989.

[9] K. Gabriel, W. Trimmer, and J. Walker, "A micro rotary actuator using shape memory alloys," *Sensors Actuat.*, vol. 15, no. 1, pp. 95–102, 1988.

[10] R. Jebens, F. Salsedo, and P. Dario, "Microactuators for aligning optical fibers," *Sensors Actuat.*, vol. 20, no. 1, pp. 65–73, 1989.

[11] J. Harrison and D. Hodgson, "Use of TiNi in mechanical and electrical connectors," in *Proc. Int. Symp. Shape Memory Effects and Applications*, 1975, pp. 517–523.

[12] V. Michaud, "Can shape memory alloy composites be smart?," *Script. Mater.*, vol. 50, no. 2, pp. 249–253, 2004.

[13] Z. Bo and D. Lagoudas, "Thermomechanical modeling of polycrystalline SMAs under cyclic loading, Part IV: Modeling of minor hysteresis loops," *Int. J. Eng. Sci.*, vol. 37, pp. 1205–1249, 1999.

[14] X. Wu, J. Wu, and Z. Wang, "The variation of electrical resistance of near stoichiometric NiTi during thermo-mechanic procedures," *Smart Mater. Struct.*, vol. 8, pp. 574–578, 1999.

[15] V. Brailovski, F. Trochu, and G. Daigneault, "Temporal characteristics of shape memory linear actuators and their application to circuit breakers," *Mater. Design*, vol. 17, no. 3, pp. 151–158, 1996.

[16] D. Madill and D. Wang, "Modeling and L_2-stability of a shape memory alloy position control system," *IEEE Trans. Control Syst. Technol.*, vol. 6, no. 4, pp. 473–481, Jul. 1998.

[17] S. Sukhatme, *A Textbook on Heat Transfer*. Hyderabad, India: Universities Press, 1996.

[18] J. McNichols and J. Cory, "Thermodynamics of nitinol," *J. Appl. Phys.*, vol. 61, no. 3, pp. 972–984, 1987.

[19] A. Bekker and L. Brinson, "Phase diagram based description of the hysteresis behavior of shape memory alloys," *Acta Mater.*, vol. 46, no. 10, pp. 3649–3665, 1998.

[20] Y. Ivshin and T. Pence, "A constitutive model for hysteretic phase transition behavior," *Int. J. Eng. Sci.*, vol. 32, no. 4, pp. 681–704, 1994.

[21] A. Likhachev, "Differential equation of hysteresis: Application to partial martensitic transformation in shape-memory alloys," *Script. Metallurg. Mater.*, vol. 32, no. 4, pp. 633–636, 1995.

[22] Y. Liu, "Detwinning process and its anisotropy in shape memory alloys," in *Proc. SPIE*, vol. 4234, 2000, pp. 82–93.

[23] A. Keefe, "Thermo-mechanical characterization of shape memory alloy torque tube actuators," Master's thesis, Univ. of California, Los Angeles, CA, 1999.

[24] A. Visintin, *Differential Models of Hysteresis*. Berlin, Germany: Springer-Verlag, 1994.

[25] T. Coleman, M. Branch, and A. Grace, "Optimization toolbox," in *User's Guide*. Natick, MA: The Mathworks Inc., 1999.

[26] Z. Bo and D. Lagoudas, "Thermomechanical modeling of polycrystalline SMAs under cyclic loading, Part I: Theoretical derivations," *Int. J. Eng. Sci.*, vol. 37, pp. 1089–1140, 1999.

Sushant M. Dutta (S'02) received the B.S. degree in mechanical engineering from the Indian Institute for Technology Bombay, Mumbai, India, in 2001, and the M.S. degree in mechanical engineering from Rice University, Houston, TX, in 2004. He is currently working toward the Ph.D. degree in mechanical engineering at Rice University.

His research interests include dynamics modeling, hysteresis in mechanical systems, shape memory alloys, and intelligent systems.

Fathi H. Ghorbel (S'86–M'87–M'91–SM'00) received the B.S. degree with honors from the Pennsylvania State University, Philadelphia, the M.S. degree from Carnegie-Mellon University, Pittsburgh, PA, and the Ph.D. degree from the University of Illinois at Urbana-Champaign, in 1985, 1987, and 1991, respectively, all in mechanical engineering.

He is an Associate Professor in the Department of Mechanical Engineering and Materials Science, Rice University, Houston, TX, where he serves as the Director of Graduate Studies. He has a joint appointment in the Department of Bioengineering. He is the Director of the Robotics and Intelligent Systems (RiSYS) Laboratory. His research is in the areas of dynamic systems and control, robotics, and biomedical engineering systems.

Dr. Ghorbel is a Member of the ASME, a member of Sigma Xi, IFAC, SIAM, IASTED, and ASEE. He is the Past Chair of the ASME Biomechanical Systems Panel, and the past Chair of the IEEE Control Systems Society's Technical Committee on Manufacturing Automation and Robotic Control. He is an Associate Editor of the IEEE TRANSACTIONS ON CONTROL SYSTEMS TECHNOLOGY, an Associate Editor of the *ASME Journal of Dynamic Systems, Measurement, and Control*, an Associate Editor for the IEEE Control Systems Society Conference Editorial Board, and a past Associate Editor of the *International Journal of Robotics and Automation*.